J. Mech. Phys. Solids 171 (2023) 105161

Contents lists available at ScienceDirect

Journal of the Mechanics and Physics of Solids

journal homepage: www.elsevier.com/locate/jmps

Tensile testing of polymers: Integration of digital image correlation, infrared thermography and finite element modelling

Peihao Song [a,b], Akash Trivedi [a,b], Clive R Siviour [a,*]

[a] Department of Engineering Science, University of Oxford, Parks Road, OX1 3PJ, United Kingdom
[b] DPI, P.O. Box 902 AX, Eindhoven 5600, the Netherlands

ARTICLE INFO

Keywords:
Polycarbonate
Tensile test
Digital Image Correlation
Thermography
Strain localisation
Viscoplastic constitutive model

ABSTRACT

Tensile tests are often used as part of material characterisation strategies; however, the observed deformation is often complex, and it can be difficult to distinguish the underlying material behaviour from the structural response of the specimen. The objective of the research in this paper was to investigate whether a more accurate calibration of a material model could be obtained by considering not just the global behaviour of the specimen, but also the local strain-time response calculated from full-field displacement information obtained using digital image correlation. Tensile experiments were performed using ISO standard, flat, dog bone specimens. Optical and infra-red imaging were used to calculate full field displacement and temperature maps, and a finite element model of the experiment was produced. These were combined with compression test data from the same material to calibrate a constitutive model, which was shown to describe well the deformation and temperature rise in the specimen. The research demonstrates that it is insufficient to use force-displacement information from tensile experiments to calibrate, or validate, constitutive models of polymers. Further, it demonstrates a more applicable method, which could be further automated in the future.

1. Introduction

Polycarbonate (PC) is a typical amorphous thermoplastic polymer, which is widely used in engineering applications because of its good mechanical properties. These properties have been extensively characterised in the past half-century. Of particular relevance are papers showing data from characterisation of the tensile and compressive response of PC at room temperature (Boyce and Arruda, 1990; Boyce et al., 1994). Results on the pressure-dependant yield stress of polycarbonate indicate that the tensile yield stress is lower than the compressive at the same strain rate (Siviour and Jordan, 2016). The deformation process in a uniaxial tension test is strongly unstable, and the instability first appears as a shear band followed by stabilized neck formation and propagation (Lu and Ravi-Chandar, 1999). This is consistent with other studies on amorphous polymers (Li and Buckley, 2009, 2010; Parsons et al., 2004; Zhang et al., 2018).

Quasi-static tensile experiments are often performed on dog-bone specimens using contacting strain gauges or extensometers for strain measurement. However, the first of these only gives strain measurements at a point, and the second the average strain in a specimen, and both are unable to give information in experiments in which necking is observed; this also prevents the calculation of true stress (Grytten et al., 2009).

* Corresponding author.
E-mail address: clive.siviour@eng.ox.ac.uk (C.R. Siviour).

https://doi.org/10.1016/j.jmps.2022.105161
Received 22 August 2022; Received in revised form 18 November 2022; Accepted 23 November 2022
Available online 28 November 2022

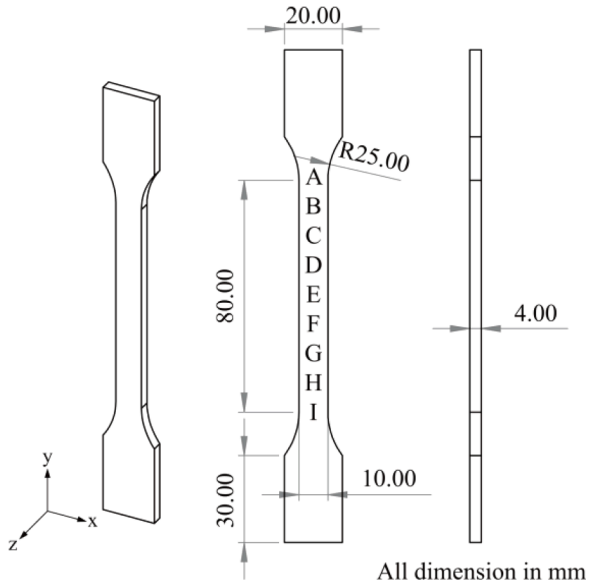

Fig. 1. Geometry of the specimens used in uniaxial tension tests. Points A to I indicate the locations at which local strain measurements were later obtained.

If suitable images of the specimen can be obtained during deformation, digital image correlation (DIC), provides a solution to measure the full-field behaviour throughout the experiment (Grytten et al., 2009; Lei et al., 2021; Parsons et al., 2004; Zhang et al., 2018). Parsons et al. (2004) performed experiments on PC in which local strain (true strain) was extracted from DIC, and the true stress was estimated using the current cross-section area, assuming the stretch ratio in transverse and through-thickness directions were the same. However, the formation of an inhomogeneous shear band and potential anisotropic deformation in the lateral and transverse directions at large strains can affect this calculation.

During the loading process, most mechanical energy is dissipated into thermal energy, while the rest of the energy is partially used for microstructural evolution (Haward, 1994), and hardening (Krairi and Doghri, 2014). The heat generated from the plastic work can cause the temperature of the material to rise. It is well known that the mechanical behaviours of polymers are temperature- and rate-dependant, thus, a temperature rise during the tests can significantly affect the mechanical response. Thermal cameras have been used to measure the temperature in uniaxial tension tests in several studies (Jordan et al., 2020; Lin et al., 2016; Shen et al., 2019). Moreover, the DIC and thermography techniques were combined to measure the temperature change and the onset of fatigue damage for a composite material (Dattoma and Giancane, 2013). Combining these contactless measuring techniques (DIC and thermal imaging) provides an opportunity to understand the interactions between thermal and mechanical behaviours, which can help build up a more accurate constitutive model.

In order to predict experiments with complex stress states (i.e. impact test), the intrinsic material properties, such as the stress-strain relationship during homogeneous deformation, should be first evaluated and described by a material model (Torres and Frontini, 2016) because the deformation in a tensile test is inhomogeneous and much more difficult to interpret than tests with homogeneous deformation (Meijer and Govaert, 2005). The investigation of constitutive models of polymeric materials started from the work of Haward and Thackray, who used models with two parallel springs to describe viscoelastic and post-yield behaviours (Haward and Thackray, 1968). Following that, many scholars developed time- and temperature-dependant thermomechanical constitutive models to interpret the constitutive behaviours of glassy polymers; commonly used models include the Boyce-Parks-Argon (BPA) model (Arruda and Boyce, 1993; Boyce et al., 1988; Hasan and Boyce, 1995), the Oxford Glass Rubber (OGR) model (Buckley et al., 2004; Buckley and Jones, 1995; De Focatiis et al., 2010), and the Eindhoven Glassy Polymer (EGP) model (Klompen et al., 2005; Tervoort et al., 1997; Van Breemen et al., 2011). One method to incorporate these into commercial Finite Element (FE) code is to generate user-defined material behaviour as a subroutine using a material library, PolyUMod® (Bergstrom, 2012), which has been used to simulate the tensile (Torres et al., 2016) and biaxial impact tests (Torres and Frontini, 2016; Torres et al., 2016). In this material library (Bergstrom, 2012), the three network model (TNM) has been explicitly developed for thermoplastic polymers and agrees well with experimental results for high density polyethylene (HDPE) (Rueda et al., 2015) and Ultra-high molecular weight polyethylene (UHMWPE) (Bergstrom and Bischoff, 2010).

The current paper presents a comprehensive study of the tensile response of polycarbonate, considering experimental data and analysis techniques. Tensile experiments were performed at speeds of 5 and 50 mm/min on flat dogbone specimens designed according to ISO 527 1A, with nominal gauge lengths of 80 mm. DIC was employed to measure the deformation field on one of the specimen surfaces. At the same time, a thermal camera was used to image the other side of the specimen to monitor the temperature field. From the DIC outputs, axial strain data were extracted from different positions on the specimen, and the stress was estimated using three different methods. A time-temperature coupled viscoplastic constitutive model (TNM) (Bergstrom, 2012; Bergstrom and Bischoff,

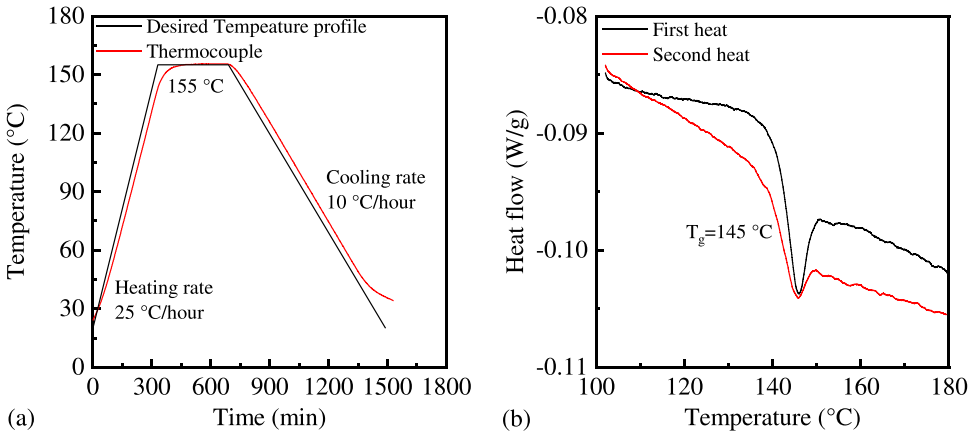

Fig. 2. (a) Annealing temperature profile (b) DSC data showing glass transition temperature.

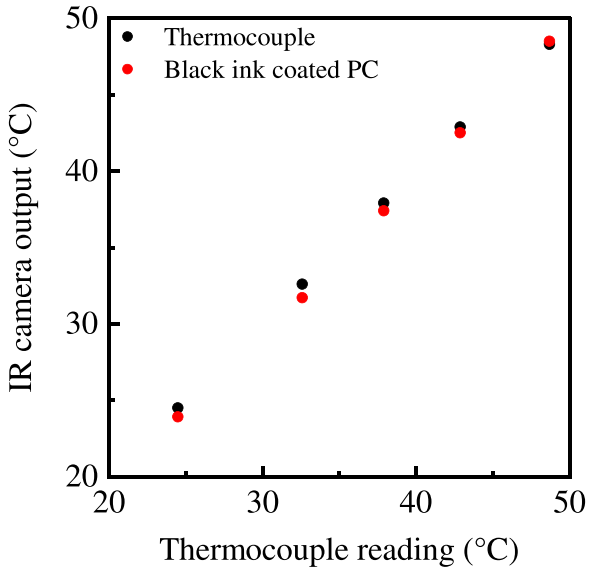

Fig. 3. Comparison of IR and thermocouple temperature readings.

2010) was used to model the large strain tension deformation process. Firstly, stress-strain data from true strain rate controlled varying rate and temperature uniaxial compression experiments were used to find material parameters. Then, an FE model of the experiment was built and used to refine the parameters through comparison with the tensile data, including the local strains and temperature rises mentioned above. At the same time, the temperature change and Taylor Quinney Factor (TQC) obtained from the experimental and numerical study are compared. Following that, parametric studies were performed to build a further understanding of the large strain related parameters. The calibrated model was shown to describe the stress-strain curves and temperature evolution very well. This study demonstrates the more general need for this fully integrated approach to obtaining constitutive data from tensile experiments on polymers.

2. Material information and sample preparation

The Bisphenol A-Polycarbonate (PC) used in this study was LEXAM™ RESIN 103R, provided by SABIC. Dogbone samples (ISO 527 1A) were injection moulded with gauge section dimensions 80 × 10 × 4 mm, as shown in Fig. 1.

To minimise the residual stress resulting from manufacturing, the specimens were annealed. The annealing profile consisted of a 25 °C/hour heat to 155 °C, which is 10 °C above the glass transition temperature (T_g ~ 145 °C). This temperature was held for six hours, following which it was decreased to room temperature at a 10 °C/hour cooling rate. During the annealing process, the specimens were sandwiched between two metal plates and a thermocouple was placed on one of the plates at a location 3 mm from the edge of the sample to confirm the temperature profile. The maximum dimension change of the samples was 1.5%, and the removal of in-

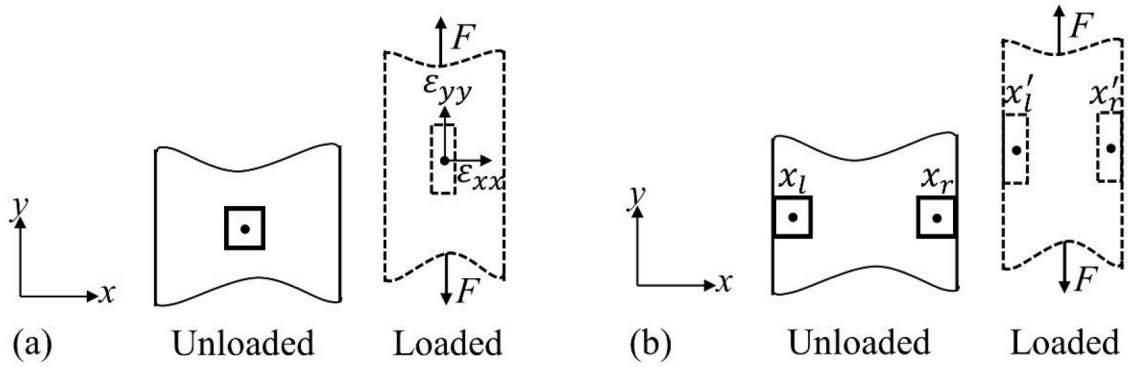

Fig. 4. Illustration of strain calculations (a) Method 1 and 2 (b) Method 3.

plane residual stress was confirmed using polarising films. The nominal heating profile, along with the thermocouple data for one of the specimens is shown in Fig. 2(a). To inform the annealing process, a TA Q2000 differential scanning calorimeter (DSC) was used to measure the glass transition temperature (T_g). Starting with unannealed material, the specimen was heated to 180 °C, then cooled back to 100 °C and heated again. The heating and cooling cycles were performed at 2 °C/min and data were recorded on both heating cycles. Data from these measurements, Fig. 2(b), indicate a glass transition temperature of 145 °C.

3. Experimental procedure

3.1. Calibration of thermal camera

PC is a transparent polymer with good infrared transmission, which is itself sensitive to thermal history and stress (Soloukhin et al., 2003). In these experiments, the emissivity was controlled by coating the specimen with black ink, which was found to deform with the specimen during loading. To confirm the value of the emissivity, a disk of material of diameter 5 mm and thickness of 3 mm was painted on one side and placed in contact with a hot plate whose temperature was measured using a thermocouple. The temperature of the hot plate was varied from room temperature to 60 °C, and the TELOPS FAST-IR M350 infrared camera used for the rest of the experiments presented in this paper was employed to read the temperature of the specimen. As shown in Fig. 3, when using an emissivity of 1, the temperature of the specimen matches the thermocouple to within ± 0.5 °C.

3.2. Testing procedure

Uniaxial tension experiments were performed on the annealed specimens using an Instron model 5582 screw-driven load frame with a 100 kN load cell at room temperature (around 24 C) and loading speeds of 50 and 5 mm/min. For the DIC measurements, a white background was produced on one face of the specimen using an airbrush, and the speckles are made by a black marker pen. Black ink was coated on the other face as described above. A Point Grey camera with a 60 mm Nikon lens was placed 960 mm from the sample surface and used to obtain images for the DIC measurements. The thermographic images were acquired by an infrared (IR) camera with a resolution of 320 × 256 pixels^2; the frame rates were 100 and 10 Hz for 50 and 5 mm/min loading speeds, respectively. The adopted DIC and IR camera settings can be found in Table A1 in Appendix A.

4. Post-processing of experiments

4.1. Strain measurements

In order to obtain displacement, strain and strain rate information, the optical images were analysed using the commercial software MatchID® (www.matchid.eu, version 2022.2.1). In particular, to help understand the strain localization and deformation processes, nine data points were selected from the centreline of the specimen at 10 mm intervals along the gauge length, labelled as points A to point I in Fig. 1. Strain data, in the form of Henkey (true) strain, were extracted at these points as functions of time, as well as from the first necking point, which occurred randomly in the gauge region.

4.2. Transverse true strain estimation and axial true stress calculation

The axial strains obtained above were then used to estimate the axial true stress at different points in the specimen. This requires an estimate of the transverse and through thickness strains, ε_{xx} and ε_{zz}. In this study, three approaches with different assumptions were used to estimate the strains and the axial stress (σ_{yy}) using each of the following methods:

In each case, it was assumed that the stretch ratio in transverse and through-thickness directions was the same: $\lambda_{xx} = \lambda_{zz}$ ($\varepsilon_{xx} = \varepsilon_{zz}$).

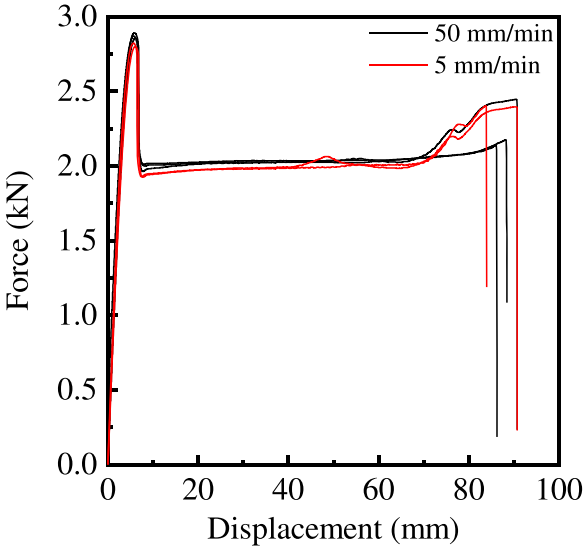

Fig. 5. Force-displacement curves for tensile experiments at crosshead displacement speeds of 50 and 5 mm/min (In all tests, the specimens are tested to failure).

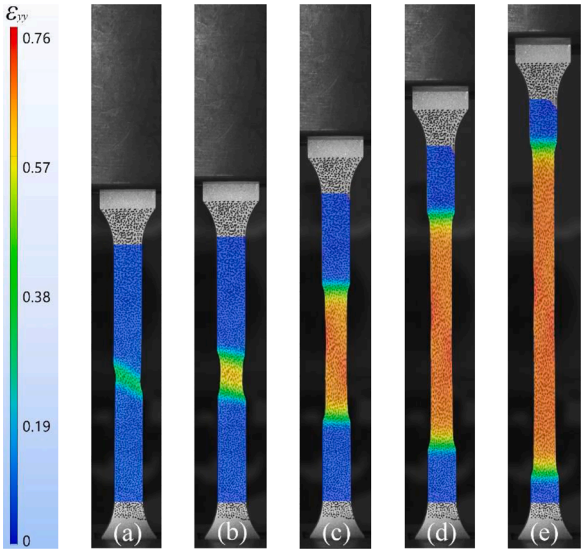

Fig. 6. True (Henky) strain maps obtained using DIC (a) Shear band initiation at 8.4 s (crosshead displacement = 7 mm) (b) unstable neck propagation at 12 s (10 mm) (c) stable neck propagation at 30 s (25 mm) (d) propagation towards the ends of specimen at 50 s (41.7 mm) (e) further propagation at 70 s (58.3 mm).

The three approaches used for ε_{xx} and σ_{yy} were:

Method 1 (Fig. 4(a)): to obtain ε_{xx} from the DIC at the same point as ε_{yy}, and calculate the stress as:

$$\sigma_{yy} = \frac{F}{A_0 \times \exp(2\varepsilon_{xx})} \tag{1}$$

Where A_0 is the initial cross-section area in the gauge area.

Method 2 (Fig. 4(a)): to calculate ε_{xx} from ε_{yy} assuming constant volume, so that:

$$\varepsilon_{xx} = \varepsilon_{zz} = \frac{-\varepsilon_{yy}}{2} \tag{2}$$

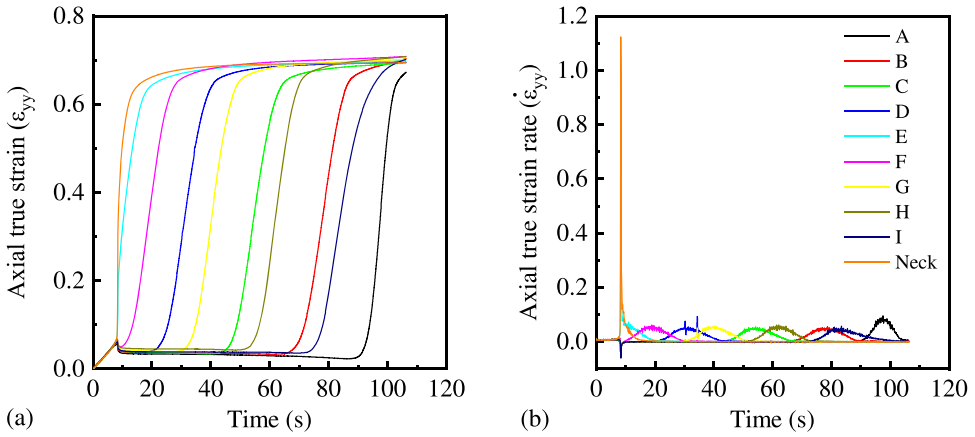

Fig. 7. Data extracted from ten points in the gauge area, nine points evenly spaced as shown in Fig. 1, plus an additional point at the location at which the neck formed (a) axial true strain vs time (b) axial true strain rate vs time. In this case, Point E was very close to Point Neck formation.

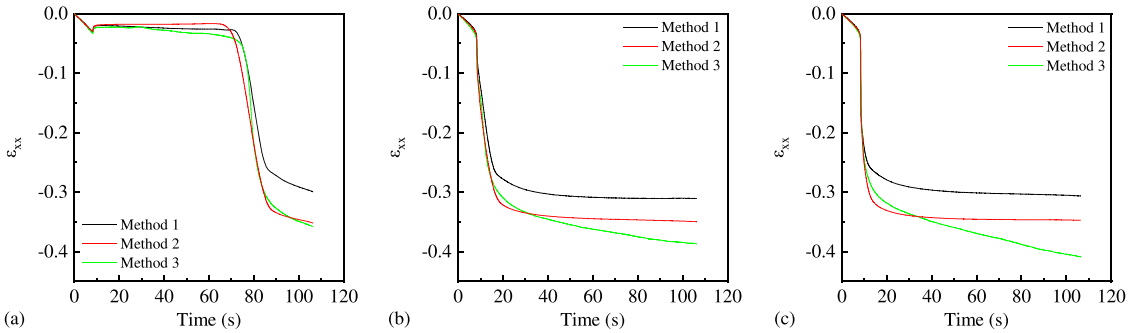

Fig. 8. Transverse true strain against time (a) Point B (b) Point E (c) Point Neck.

$$\sigma_{yy} = \frac{F \times \exp(\varepsilon_{yy})}{A_0} \tag{3}$$

Method 3 (Fig. 4(b)): to estimate ε_{xx} and ε_{yy} using data from the edge of the specimen as:

$$\varepsilon_{xx} = \ln\left(\frac{x_r' - x_l'}{x_r - x_l}\right) \tag{4}$$

$$\sigma_{yy} = \frac{F}{A_0 \times \exp(2\varepsilon_{xx})} \tag{5}$$

5. Experimental results

5.1. Force-displacement curves and optical images

Several tests were conducted for each loading speed; the load-displacement curves obtained are shown in Fig. 5. In this paper, one of the 50 mm/min tests is used as an example to illustrate the results and data analysis process; the numerical results presented in the next section are also based on this test.

Fig. 6 shows contours of axial true strain calculated using DIC for a 50 mm/min tension test at different times. The specimen experiences necking initiation, unstable neck propagation and steady necking propagation in succession, following which the neck extends to the whole specimen, the stress rises rapidly, and failure occurs.

5.2. Axial strain and strain rate

Fig. 7 shows strain and strain rate data extracted as functions of time for 10 locations on the specimen gauge length (Point A to I indicated in Fig. 1, and Point Neck which occurred between Point E and F, this point was picked at the location of initial shear band formation, and in the centre of the specimen width). In Fig. 7(a), the specimen is shown to deform homogeneously at axial true strain

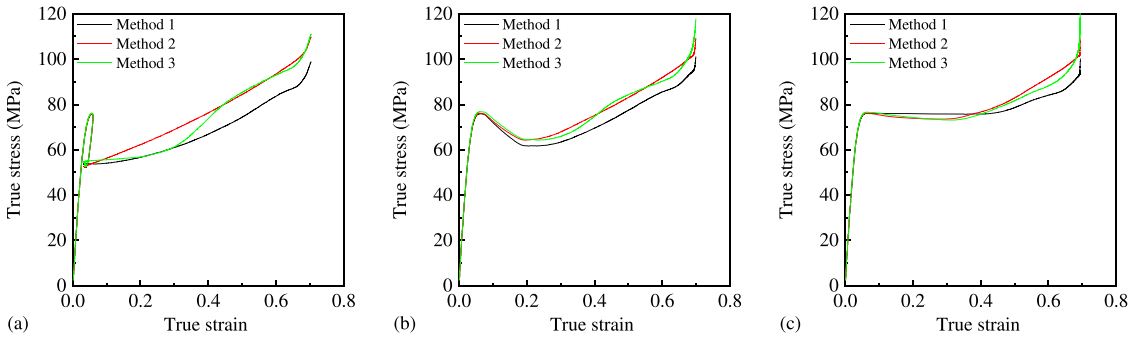

Fig. 9. Uniaxial true stress-true strain curves, (a) Point B (b) Point E (c) Point Neck.

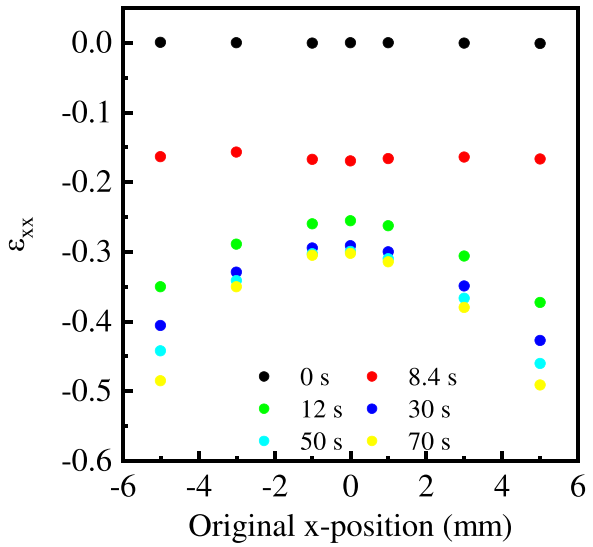

Fig. 10. Transverse true strain against position for seven points in the line of the Point Neck.

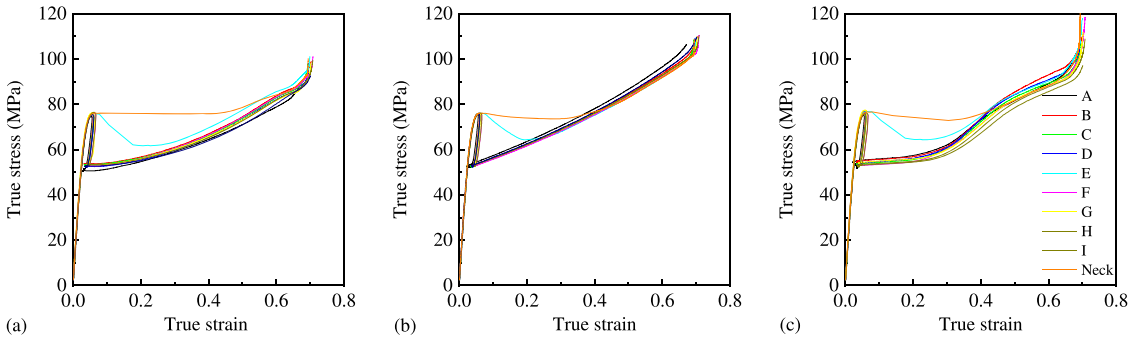

Fig. 11. Uniaxial true stress vs true strain curves, (a) Method 1, (b) Method 2, (c) Method 3.

less than 0.06; however, once necking begins, the curves diverge. Close to the initial localisation, there is a very rapid increase in strain rate as the neck forms, whilst points distant from the neck experience a small drop in strain associated with the decrease in the force supported by the specimen, and resulting recovery of some of the elastic strain. As the neck progresses through the specimen, more distant points experience a rapid increase in the strain as they progress from elastic to plastic deformation, but the rates are not as high as at the Point Neck formation, where the speed of necking is greatly increased by the relaxation of elastic strain elsewhere in the specimen and load chain. These data, combined with the displacement maps in the previous section, indicate why it is necessary to obtain full-field information rather than relying on overall force-displacement data to calibrate constitutive models.

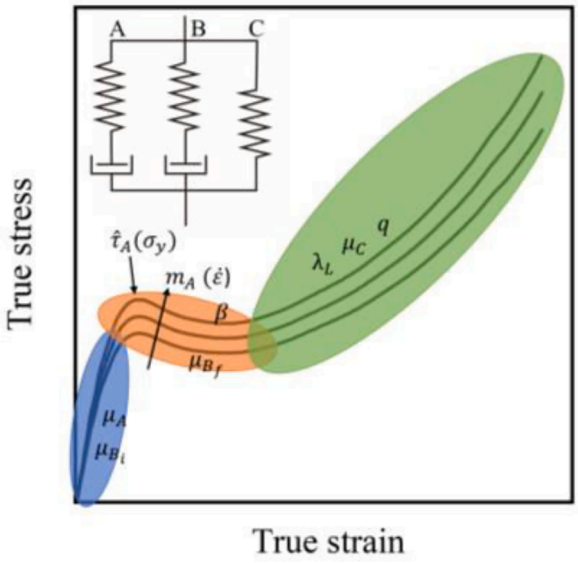

Fig. 12. Schematic of three-network model, and illustration of where the model parameters (Table 1) affect the stress-strain response.

Table 1
Material parameters for three-network model used in Abaqus/Standard.

Quantity	Fit to compression (Set 1)	Final to compression (Set Final)
Material parameters of PC		
Density, ρ	1.08 g/cm^3 (SABIC, 2021)*	
Shear modulus of network A, μ_A	271.1 (MPa)	308.9 (MPa)
Locking stretch, λ_L	9.9	2.2
Bulk modulus, κ	4.4 (GPa) (Knauss and Zhu, 2002)	
Flow resistance of network A, $\hat{\tau}_A$	31.8 (24 °C)/ 27.5 (60 °C) (MPa)	38.5 (24 °C)/ 33.5 (60 °C) (MPa)
Pressure-dependant of flow, a	0.1	
Stress exponential of network A, m_A	40	
Initial shear modulus of network B, μ_{Bi}	271 (MPa)	233.2 (MPa)
Final shear modulus of network B, μ_{Bf}	7.7 (MPa)	13.5 (MPa)
Evolution rate of μ_{Bi}, β	14	18.2
Flow resistance of network B, $\hat{\tau}_B$	92.7 (MPa)	62.3 (MPa)
Stress exponential of network B, m_B	14.3 (MPa)	21.1 (MPa)
Shear modulus of network C, μ_C	2.5 (MPa)	5 (MPa)
Relative contribution of I_2 of network C, q	0	2
Thermal properties for PC		
Temperature factor, $\hat{\theta}$	0	
Temperature exponential, n	0	
Thermal expansion coefficient, α	0	
Thermal expansion reference temperature, θ_0	24 °C	
Specific heat capacity, C_p	1.065 J/ (g °C)	
Thermal conductivity, K	0.2 W/(m K) (SABIC, 2021)	
Inelastic heat fraction, Taylor Quinney Factor (TQC)	0.9*	
Absolute zero temperature	−273 (°C)	
Stefan-Boltzmann constant	5.67×10^{-8} (kg s^{-3} K^{-4})	
Emissivity of black ink	0.99	

* In the product property report (SABIC, 2021), the value of density (ρ) is 1.2 g/cm^3; at the same time, in this project all plastic work is assumed to be converted to heat during the large strain deformation, thus, the inelastic heat fraction (TQC) is 1.0. However, the default value of TQC in Abaqus/standard is 0.9, which cannot be changed using the current user-defined material model. According to the formula for simulating the temperature rise, $\Delta T = \frac{TQC}{\rho C_p}\int_0^{\varepsilon_{yy}} \sigma d\varepsilon_p$, lowering the density and using the default TQC of 0.9 provides the same effect as TQC = 1 with normal density when simulating the temperature rise.

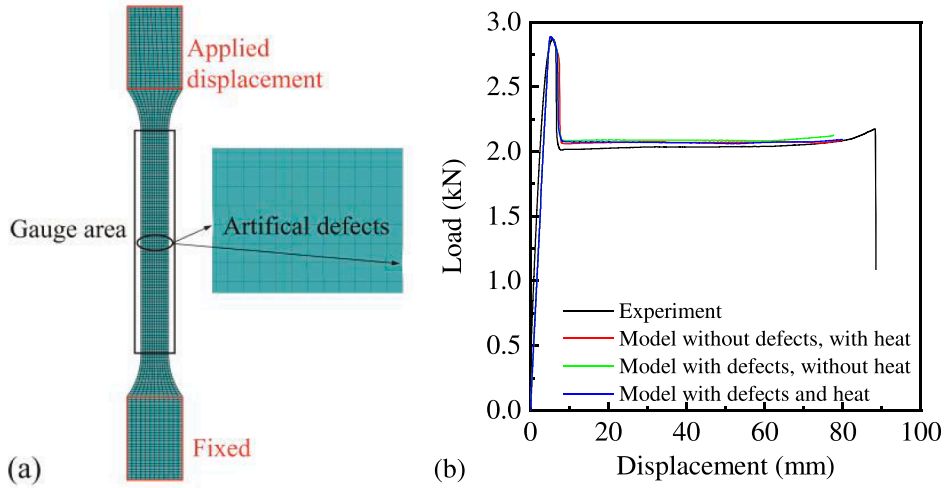

Fig. 13. (a) Mechanical and thermal boundary conditions on the tensile specimen (b) Load-displacement curves comparison between experiment and model with different assumptions: with and without defects and with and without heat effects (thermal radiation and heat conduction).

5.3. Transverse strain and uniaxial stress approximation

Using the methods discussed in the previous section, transverse strain-time data were calculated. Data from three points, Point B (far from neck initiation area), Point E (near neck initiation area) and Initial neck, on the specimen are shown in Fig. 8 as examples. It is observed that the transverse true strains are inconsistent with each other, explored further below. The true stress-strain curves for the same points are plotted in Fig. 9, and the results obtained from these three methods are again shown not to agree at large strains.

To further understand the inconsistency of transverse true strain and true stress obtained using three different methods, the transverse true strain obtained directly from DIC is plotted against a horizontal position along a line through the centre of the initial neck, at a number of different times, Fig. 10. Before necking, the value of ε_{xx} is the same at all points. Later on, however, the points closer to the edge experience larger transverse strains than those in the centre. This is consistent with the larger strains calculated using Method 3 above. It is noted that in this figure, the strains shown at $x = 0$ are equivalent to the 'Method 1′ strains. The differences between Methods 1 and 2 may be errors owing to them being based on a single DIC location, or to the incompressibility assumption used in Method 2.

Using these three methods, true stress-strain curves were produced for the 10 axial locations considered above (Point A-I and Point Neck) in Fig. 11. The curves obtained before yield are the same for the three different approaches; however, there are significant differences after yield. On the other hand, the stress-strain curves for different points on the specimen are very similar, apart from the Point Neck and Point E nearby. At these two locations, the strain increases very rapidly after yield, and within a few seconds, re-joins the other stress-strain curves at a much larger strain. The other points tend to move more slowly along the curve, as expected from the lower strain rates observed in Fig. 7. Fig. 11 also shows the unloading of these points during the force drop that accompanies initial necking. Owing to the viscoelastic nature of the material, this does not exactly follow the initial loading path.

As well as the discrepancies from the different strain calculations, there is no way to accurately verify whether the strains in the transverse and through-thickness directions are the same. Thus, finite element (FE) simulations are required to better interpret the large strain data.

6. Numerical model

6.1. Constitutive model summary

The three-network model (TNM) (Bergstrom, 2012) was used to describe the tensile deformation behaviour of the polycarbonate. In this viscoplastic model, the stress is decomposed into three parallel networks: both network A and network B consist of an elastic and viscoplastic components, whilst network C is an elastic spring, as shown in Fig. 12. The model behaviour is governed by a number of parameters, which affect the stress-strain behaviour as outlined in Fig. 12 and Table 1. The implementation of this model is described in Appendix B, and the reader is referred to the literature for more detailed information (Bergstrom, 2012, 2015).

6.2. Finite element model

A finite element (FE) model was built using a commercial FE software Abaqus/standard (Manual, 2021). The Three Network Model model was incorporated in Abaqus as a user material subroutine (UMAT) using the PolyUMod® material library (Bergstrom, 2012). Eight-node thermally coupled brick, trilinear displacement elements (C3D8T) were used with a 1 mm global mesh size with 8256

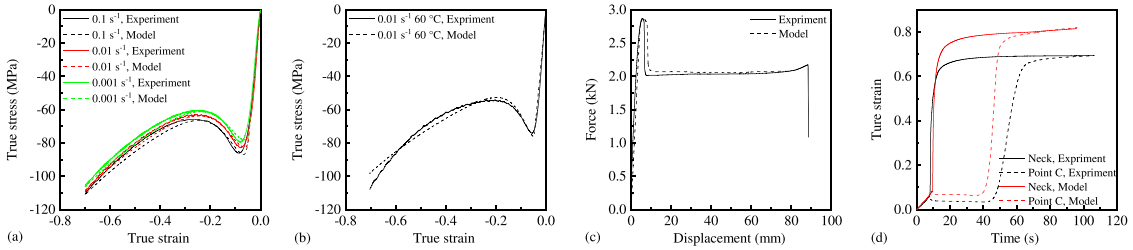

Fig. 14. Constitutive model using parameter Set 1 compared to (a) rate-dependant compression tests, (b) temperature-dependant compression tests; experimental and simulation results showing (c) load-displacement curve (d) axial true strain - time curve.

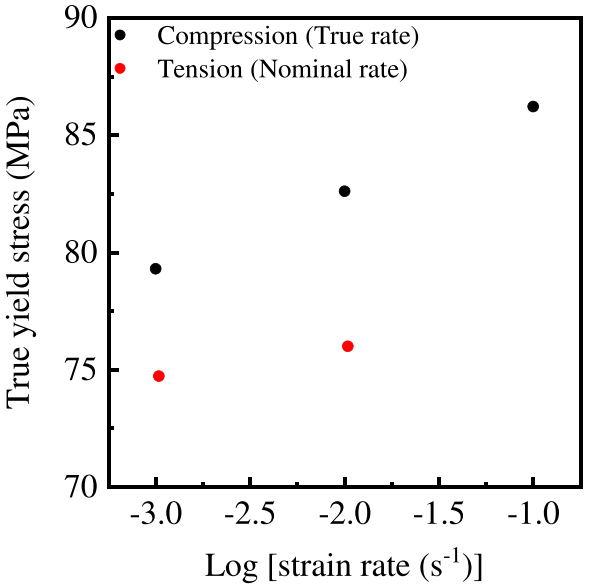

Fig. 15. Compression and tension yield stress against strain rate.

elements. The final results obtained were found to be independent of mesh size for global mesh sizes of 0.8, 1, 1.3 and 2 mm (Appendix C). As Fig. 13(a) shows, one end of the specimen is fixed, and a tensile displacement was applied on the other end. The temperature was set as 24 °C to match the experiment, and the thermal conduction and radiation are enabled to capture the heat dissipation during the large strain deformation process. In order to trigger the shear band in the FE model, small artificial material or geometric defects have been utilized in many previous numerical studies (Kweon and Benzerga, 2013; Li and Buckley, 2009, 2010; Parsons et al., 2004; Tvergaard et al., 1981; Wu and van der Giessen, 1995) to form the shear band or strain localization, and the authors state that there is no significant effect on the post-localisation results. In our study, two 0.05 mm deep symmetric perturbations in the *x*-direction were created; these artificial defects are small enough to have no significant effect on the post-yield behaviours: a comparison of force-displacement curves with and without defects are plotted in Fig. 13(b).

6.3. *Determination of constitutive parameters - Step 1: compression experiments*

It is challenging to obtain the material parameters directly during the tensile tests because of the necking instability. Therefore, true strain-rate controlled compression experiments were performed at varying rates and temperatures, and the data obtained were used to determine initial material parameters in the constitutive model.

The varying rate compression test data in Fig. 14(a) were used to estimate the initial parameters. Firstly, the sum of μ_A and μ_{Bi} is used to fit the stress-strain curve before yield. Because elastic modulus at room temperature is not very sensitive to the strain rate, over the experimental range of rates and temperature (Dynamic Mechanical Analysis (DMA) data demonstrating this are shown in Appendix D), a constant summed value of μ_A and μ_{Bi} were used to simulate the pseudo-linear-elastic behaviour. As a starting approximation, the individual values of μ_A and μ_{Bi} were made equal, as shown in Table 1 Set 1.

The value of $\widehat{\tau}_A$ was determined by fitting to the rate dependence of the yield stress, and the pressure-dependence parameter a can be determined from,

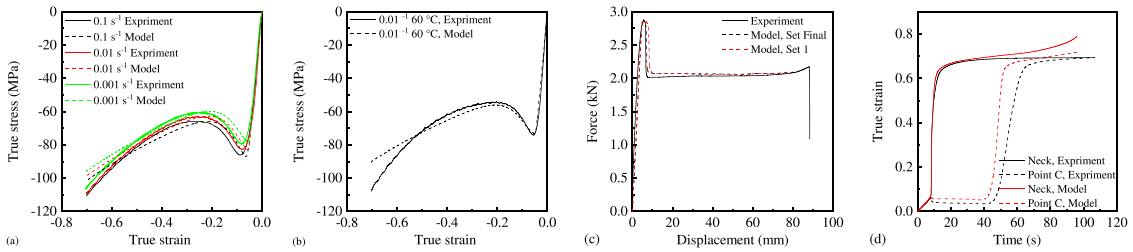

Fig. 16. Constitutive model using parameter Set Final compared to (a) rate-dependant compression tests (b) temperature-dependant compression tests; experimental and simulation results showing (c) load-displacement curves (d) axial true strain-time curve.

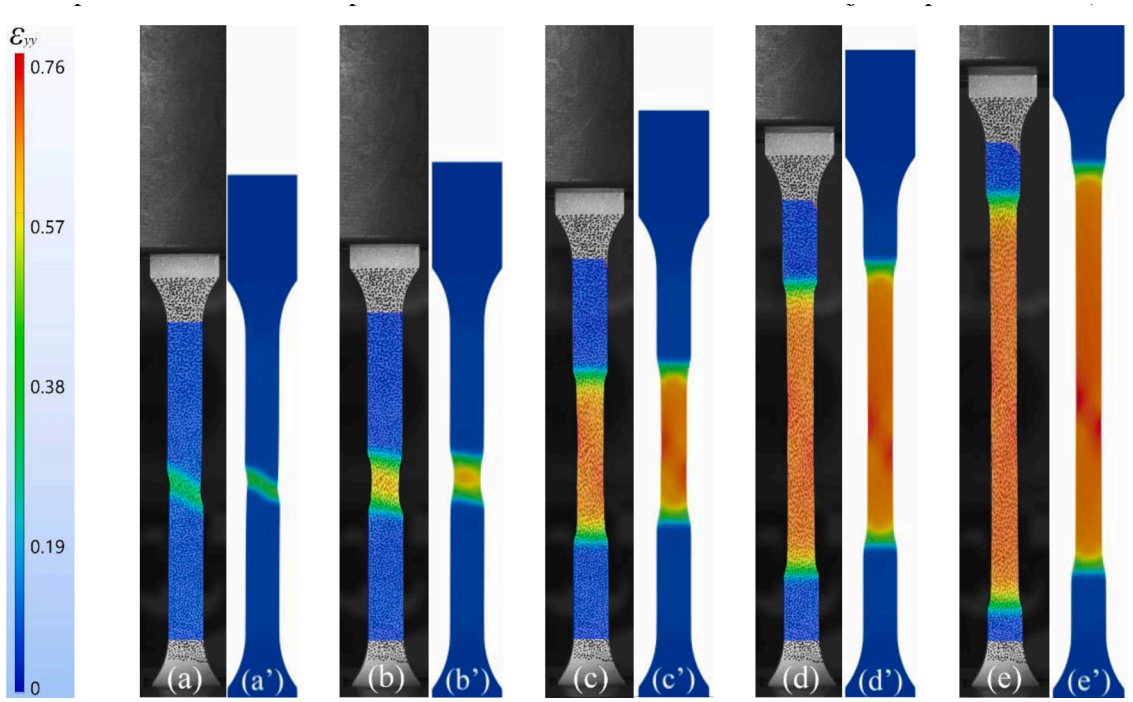

Fig. 17. Comparison of model and experimental axial strain data at 8.4, 12, 30, 50, 70 s: (a) to (e) axial strain obtained from DIC; (a') to (e') axial strain obtained from FE model.

$$\frac{|\sigma_{cy}|}{\sigma_{ty}} = \frac{3+a}{3-a} \tag{6}$$

where, σ_{cy} and σ_{ty} are compression and tension yield stresses presented in Fig. 15. The rate-dependant post-yield behaviour is determined by m_A. The strain-softening process is dominated by μ_{Bf} and β in network B, and the strain-hardening at large strains is defined using parameters λ_L, μ_C and q; these parameters were fitted to the compression curves using PolyUMod, which uses a minimization algorithm based on the Nelder-Mead simplex methods (Bergstrom, 2012; Bergstrom and Bischoff, 2010).

In the TNM, temperature dependence is usually incorporated by multiplying the whole stress-strain relationship by $\left(\frac{\theta}{\theta_0}\right)^n$, however, this changes the whole curve, including the modulus. The modulus of polycarbonate between room temperature and 60 °C is approximately constant (Appendix D and Fig. 14(a)). The $\widehat{\tau}_A$ in compression tests at 60 °C is changed to fit the yield stress without modifying other parameters in this model, as shown in Fig. 14(b). The specific heat capacity C_p was obtained from Modulated Differential Scanning Calorimetry (MDSC) using the low mass T-zero pan (Appendix E).

These parameters were then used in the simulation of the tensile experiment. The results obtained show excellent agreement with the global load-displacement curve (Fig. 14(c)); however, they do not correctly describe the local strain-time curves of different points, Fig. 14(d). Hence, further parameter refinement was performed.

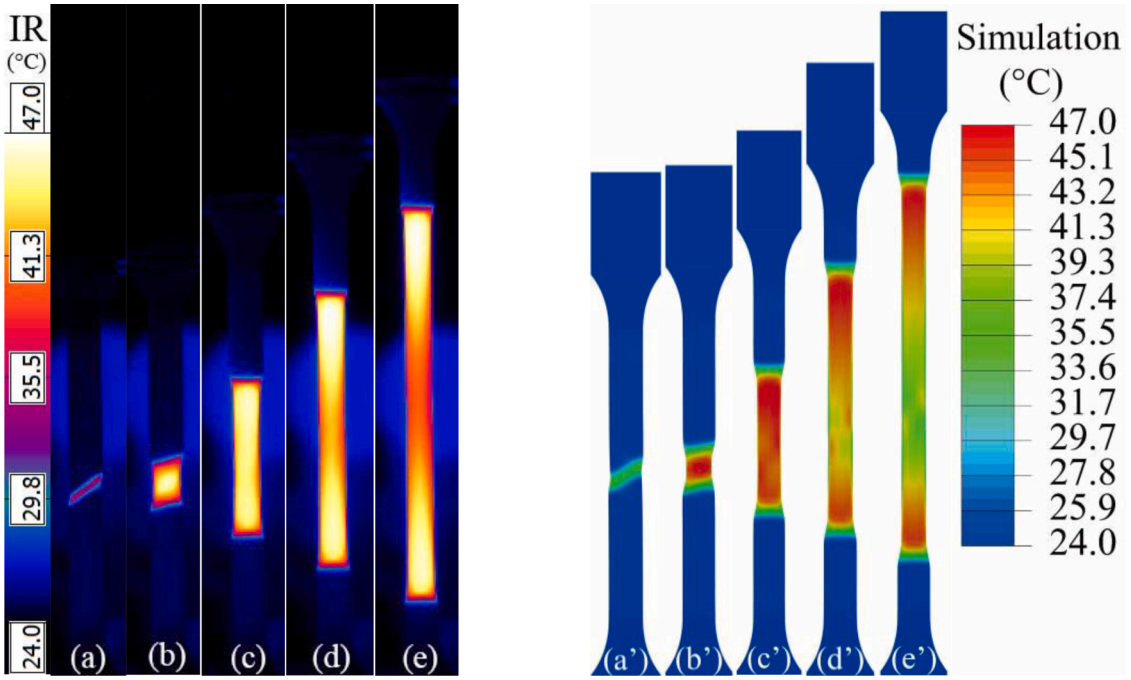

Fig. 18. Comparison of model and experimental data at 8.4, 12, 30, 50, 70 s, (a) to (e) Experimental temperature change obtained from IR camera; (a') to (e') Numerical temperature change extracted from FE model.

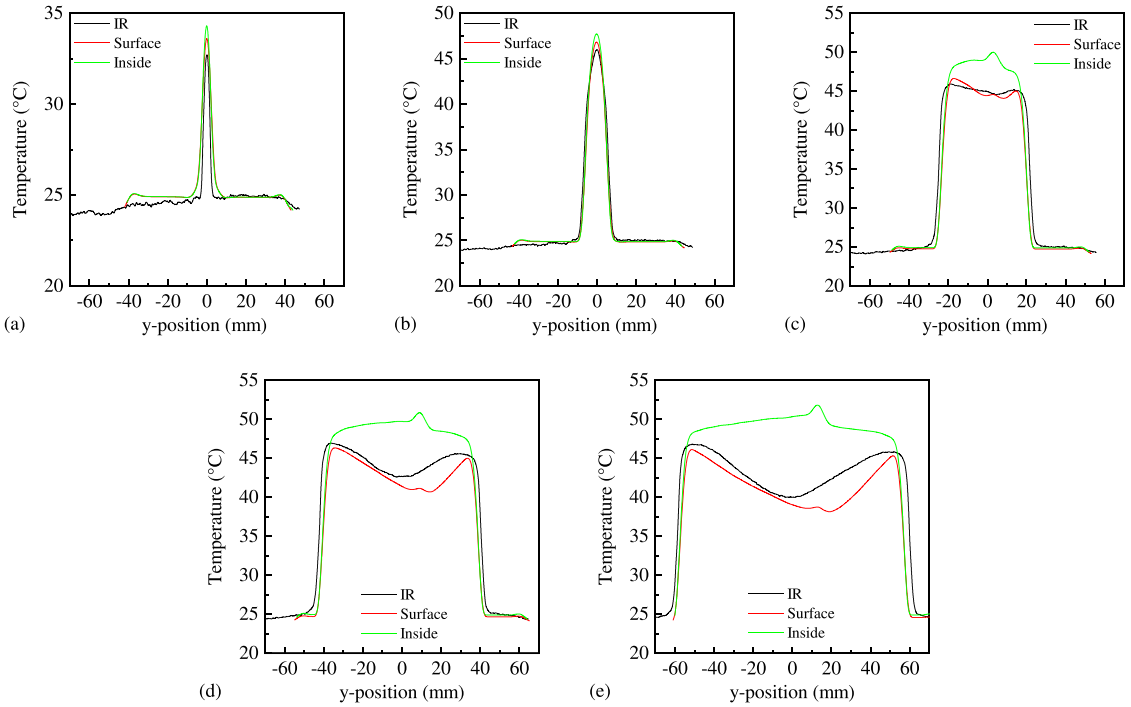

Fig. 19. Experimental (IR) and numerical (surface, inside) temperature profile down the centre of the gauge area at (a) shear band first occurring at 8.4 s (b) unstable neck propagation at 12 s (c) stable neck propagation at 30 s (d) neck extension to both ends at 50 s (e) 70 s.

6.4. Determination of constitutive parameters - Final values

After the initial fit of the material parameters, the parameter set was updated manually to better fit the tensile experiments. Some of the values derived above were kept constant: the sum of the shear moduli (i.e. $\mu_A + \mu_B$, but not the moduli themselves), the bulk modulus κ, the pressure-dependence of flow (a), the stress exponential of network A (m_A) and the thermal properties. In addition, the stress reduction caused by temperature rise is simulated using reduced $\widehat{\tau}_A$.

After some trials, the resulting material parameters, which are able to fit the global (Fig. 16(c)) and local (Fig. 16(d)) behaviours, are listed in Table 1, as Set Final. Fig. 16 also shows the compression curves implied by these parameters. The key observation here is that modifying the parameters has made little difference to the overall force-displacement curve, but has significantly improved the local strain-time curves. This is expected because the force is determined by the stress required to propagate plastic displacement along with the specimen; at all times, this displacement moves into a region of the specimen in which the strain is the same and the temperature is equal to the initial, ambient temperature: the only material parameter affecting the propagation is the initial yield stress. Hence, the force-displacement curve is a poor validation of constitutive response. As shown in Fig. 16(c), the models predicted using parameters Set 1 and Set Final give a very similar response in load-displacement, and they are consistent with the experimental results well. However, the local strain-time curves in Fig. 16(d) present good agreement with experimental results, not like the simulation results shown in Fig. 14(d). A parametric study of large-strain behaviour related parameters are shown in the next section and Appendix F.

6.5. Further comparison between experimental and simulation results (final parameters)

In the experiment, the shear band initiates at 8.4 s (Fig. 17(a)), and the strain quickly jumps to 0.35; the numerical model (Fig. 17 (a')) agrees well with the DIC results. Following the initiation of the strain localization, the specimen experiences an unsteady necking propagation, Fig. 17(b), (b'). After that, the shear band propagates stably towards both ends of the specimen as it is further deformed; at 30 s, the unsymmetrical shear band has evolved into a steadily propagating symmetrical neck, Fig. 17(c), (c'), which continues to extend. In all cases, the FE simulation agrees well with the experimental measurements. Lu and Ravi-Chandar demonstrated the process of neck formation from micro shear bands in polycarbonate (Lu and Ravi-Chandar, 1999). The macroscopic behaviour of their specimens was similar to that observed in the current study.

Considering the temperature rises, a comparison of the experimental and numerical temperature profiles are plotted for different times in Fig. 18. Images in Fig. 18 indicate good agreement between the experiment and model, with a rapid rise in temperature just behind the plastic deformation front, but the centre of the specimen cooling radiatively as the experiment progresses.

In order to perform more quantitative comparisons, temperature data were extracted from a line down the centre of the specimen and the model, Fig. 19. For the model, the surface temperature is shown along with the internal temperature extracted from the middle of the specimen (i.e. between the second and third of the four elements). These are different because of the temperature gradient needed to support radiation from the specimen surface. The y-positions are given with reference to the position of the first necking point. In Fig. 19(a), the model outputs agree well with the experimental data when strain localization occurs at 8.4 s. The inelastic area becomes broader as the shear band propagates, and the 'hot area' extends correspondingly. At 12 s, all three sets of data show a small peak, corresponding approximately to the first necking area, but the effect of the radiation is already visible in the difference between the surface and internal temperatures from the simulation.[1] At 30 to 70 s, the surface temperature in the simulation shows similar behaviour to the experiment: the temperature at the first necking area drops due to radiation from the specimen surface. Even though the specimen continues to deform, the plastic deformation rate is minimal here, so there is almost no heat generation. The exact value of the surface temperature from the FE model is a very good match to the experiment. Discrepancies may be due to one of the thermal parameters, particularly the assumed conversion of plastic work to heat; it is also possible that the specific heat capacity or thermal conductivity changes with either temperature or strain.

6.6. Investigation of large-strain parameters

A parametric study was performed for the large strain behaviour of the three-network model since the elastic modulus and temperature-, rate-, and pressure-dependant yield stresses fit well with the experimental data. The parameters investigated were locking stretch (λ_L), final shear modulus of network B (μ_{Bf}), evolution rate of μ_B (β), shear modulus of network C (μ_C) and relative contribution of I_2 of network C (q). Their values were changed in turn by ±25% from those in Table 1 'Set Final', and the strain-time data for two points on the specimen was compared, in addition to the global force-displacement curves.

The effects of varying λ_L are shown in Fig. 20(a) and (a'). The load-displacement curves are very similar apart from the one produced at the largest value. As expected, the initial value of λ_L equalling 2.2 gives the best fit to the experimental results; the timing of the strain increase at point C does not perfectly match the experiment because the necking propagation is not symmetrical in the experiment. Furthermore, for large values of λ_L (which implies less strain hardening), a second necking instability can form at the

[1] The temperature difference between the surface of the specimen and the centre may seem large, but is consistent with the gradient required to support radiation from the specimen surface. For a surface temperature of 40 °C and an emissivity of 1, the radiation is calculated from the Stefan-Boltzmann constant σ as $\sigma T^4 = 5.7 \times 10^{-8} \times 313^4 = 550$ W m^{-2}. At 60 s the temperaure difference at the centre is approximately 8 °C over a distance of 2 mm. This implies a heat flow of $k\ \Delta T/\Delta x = 0.2 \times 8 / 0.002 = 800$ W m^{-2}, which is reasonably consistent.

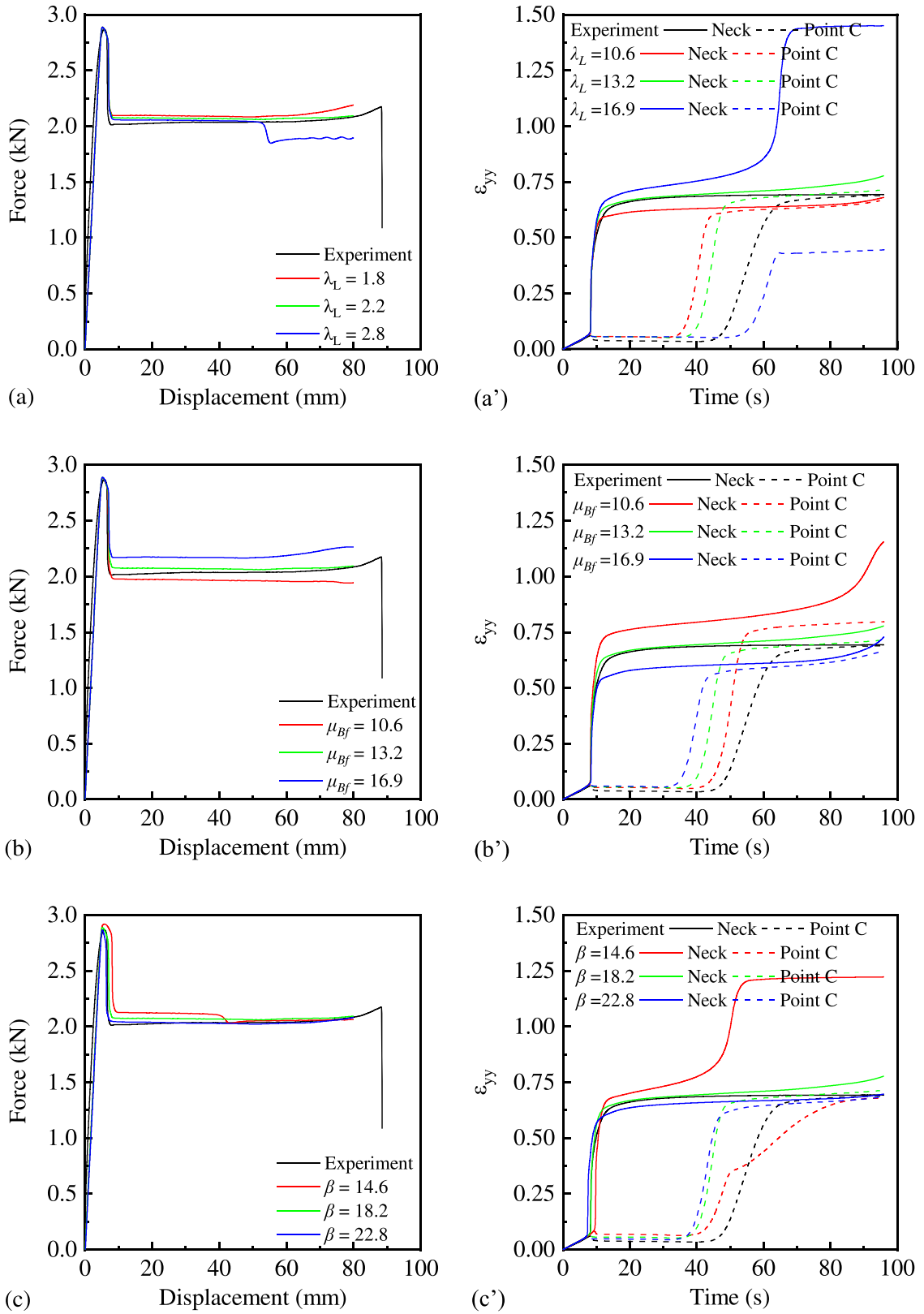

Fig. 20. Effects of λ_L (a), (a'); μ_{Bf} (b), (b'); and β (c), (c') on the load-displacement and strain-time curves.

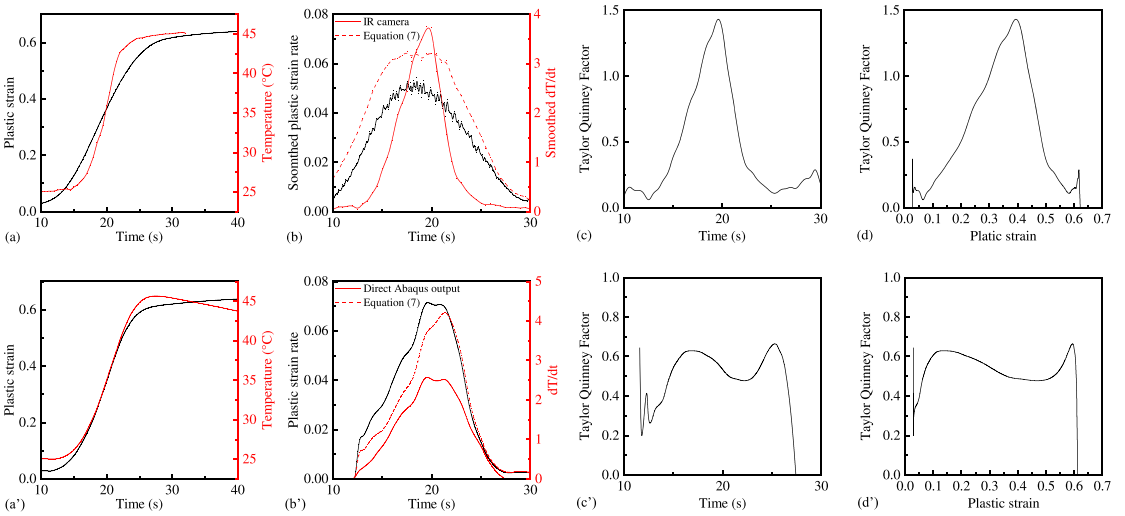

Fig. 21. Experimental ((a) to (d)) and numerical ((a') to (d')) thermal behaviours of Point F.

Table A1
Digital Image Correlation and Infrared camera Setup.

Loading speeds (mm/min)	50	5
Adopted Digital Image Correlation (DIC) Setup		
Camera (Point Grey)	GS3-U3–41C6M-C	GS3-U3–120S6M-C
Image resolution (pixel)	2048×2048, 10-bit	4240×2824, 14-bit
Frame rate (frame/s)	10	2
Lens	Nikon 60 mm Lens	
Field of view (pixels)	288×2048	380×2824
Pixel to mm conversion	0.01010	0.06135
Stand-off distance (mm)	960	
Speckle size (pixels)	≈ 7	≈ 10
DIC software	MatchID, version 2022.1.1	
Image filtering	Gaussian, 5 × 5 pixel kernel	
Subset size (pixel)	21	25
Step size (pixel)	5	3
Subset shape function	Quadratic	
Matching criterion	Zero-normalized sum of square differences (ZNSSD)	
Interpolant	Bicubic polynomial interpolation	
Strain tensor	Hencky (True) strain tensor	
Estimates progress history	Spatial and updated reference	
Strain window size	15×15 pixels^2, Quadratic Quadrilateral	
Adopted Infrared (IR) camera Setup		
Camera	Telops Fast-IR M350	
Exposure time	1000 μs	
Frame rate (frame/s)	100	10
Field of view (pixel)	180×512	
Resolution and bit depth	96×96 (dpi), 24-bit	
Pixel to mm conversion	0.4	
IR software	IR reveal, version 2022. 2. 1	

location of the first neck, which is interesting but not observed in the experiment.

The residual shear modulus of network B, μ_{Bf} controls the strain-softening process. In Fig. 20(b) and (b'), the magnitude of the force drop increases with the lower μ_{Bf} Further, the inflection point of the strain-time curve occurs later, and the final strain is larger because it becomes more difficult for the plastic deformation to propagate (the force is lower), so the material deforms to a larger strain post-yield to achieve a high enough stress.

The evolution rate of shear strength of network B (β) controls the speed of stress decrease from yield stress to the lowest peak stress after yield. To understand the influence of β on large strain deformation, two values of 14.6 and 22.8 are added to compare with the initial value of 18.2 in parameter Set Final. Lowering β (14.6) can increase the peak force and delay the yield occurring, as presented in Fig. 20(c) and (c'). In contrast, an increase of β can cause a lower peak force and bring the yield forwards because the softening area is narrowed. The forces obtained from three different values of β overlap when the model is stretched around 40 mm. This results from the value of residual strength of network B: μ_{Bf} is kept constant when investigating the effects of β. Interestingly, for small values of β, a second necking instability can be observed at the location of neck initiation, which is not observed in the experiment.

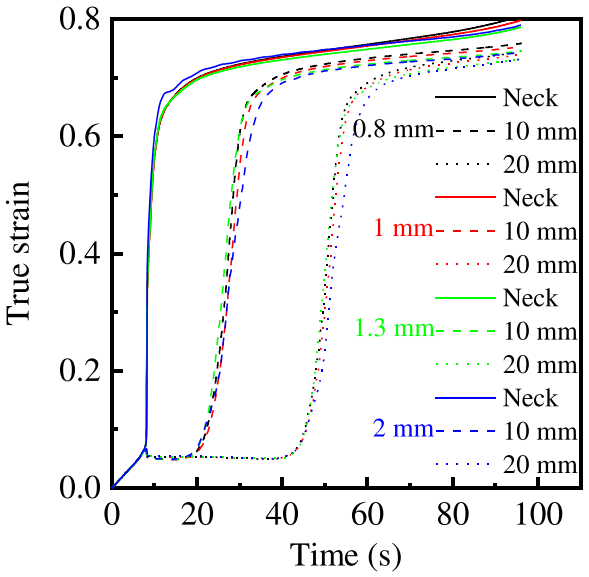

Fig. C1. Mesh sensitivity using C3D8T elements of four different sizes.

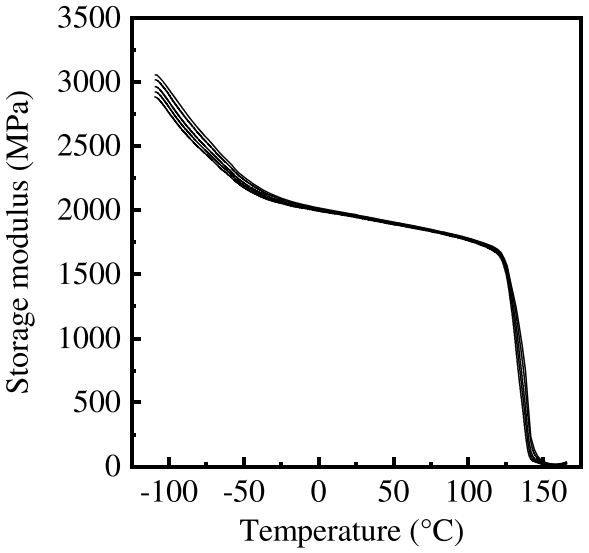

Fig. D1. Data from DMA experiments performed using single cantilever beam specimens at frequencies from 0.5 to 10 Hz and temperatures from −110 to 180 °C.

The network C related parameters: the shear modulus of network C (μ_C), and relative contribution of I_2 of network C (q) are discussed in Appendix F.

7. Discussion

The results above have presented an integrated method for fitting a constitutive model for polycarbonate to compressive and tensile experiments, and in particular, have shown that the global force-deformation behaviour is not sensitive to many of the model parameters, meaning that the fit is further enhanced by the use of local strain fields, in this case, obtained from DIC. Further, temperature maps have also been obtained. These temperature maps provide a further opportunity to examine the conversion of work to heat in the specimen. Whilst a full analysis (Maquin and Pierron, 2009) is beyond the scope of this research, it is instructive to make a simple comparison of the experimental and FE data.

Fig. 21 shows the steps required to calculate the so-called Taylor-Quinney factor (TQC), the fraction of plastic work converted into heat using data from the experiment and the final Abaqus simulation. In this case, the so-called differential value is calculated. This

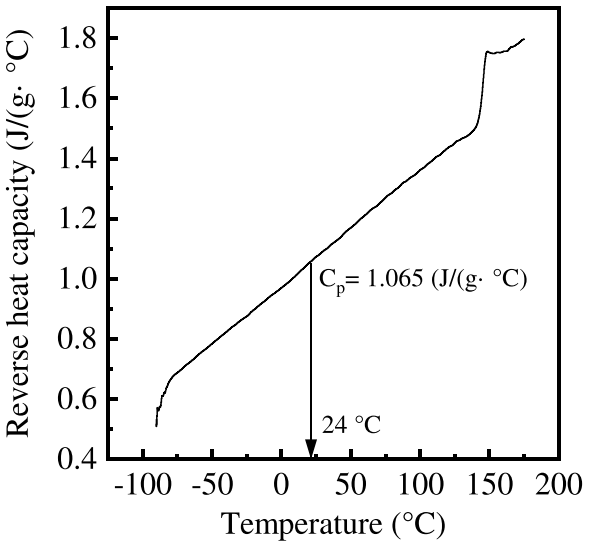

Fig. E1. MDSC test for PC using T-zero pan with 2 °C/min temperature increment and ±0.6 °C amplitude.

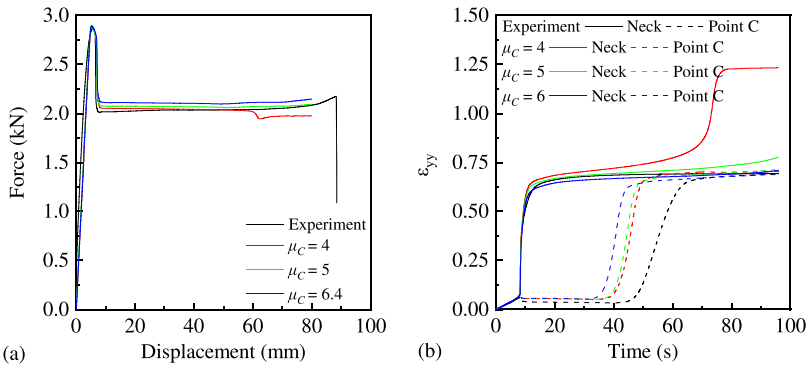

Fig. F1. Effect of changing μ_C on the large strain deformation.

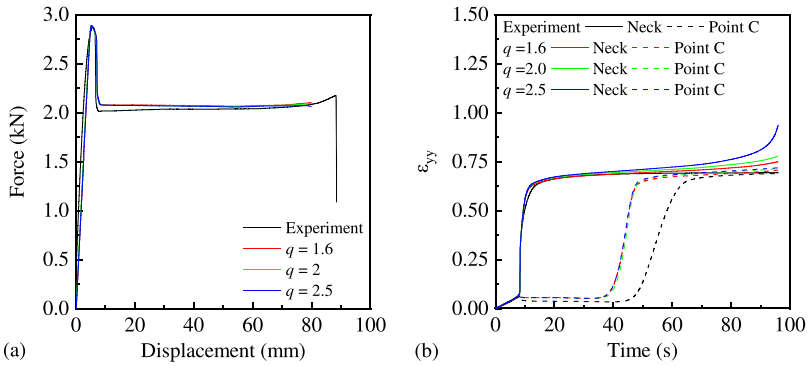

Fig. F2. Effect of q on the large strain deformation.

represents the instantaneous conversion of work to heat. Firstly, in Fig. 21(a) and (a'), the plastic strain and temperature are obtained for a location on the specimen. In this case, it is point F in Fig. 1. Whilst it is initially tempting to perform these calculations at the location of the initial neck, the very high instantaneous strain rate during neck formation makes this more challenging experimentally: imaging speeds of order 1000 frames per second would be required to obtain sufficient data, and the bandwidth of the load cell (and load chain) would probably be insufficient for the stress measurements.

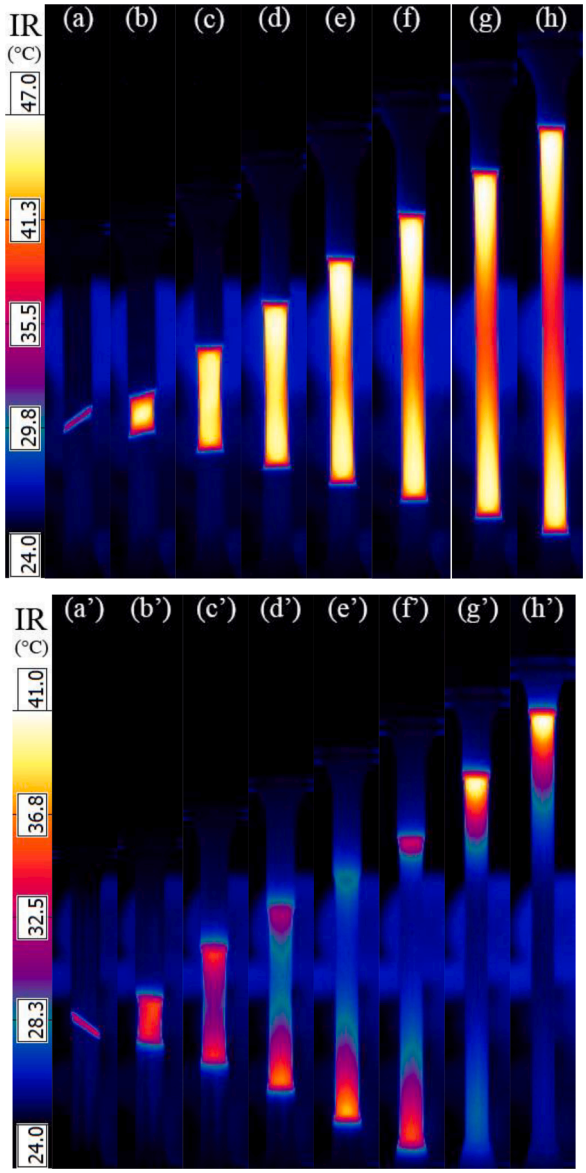

Fig. G1. Thermal mapping obtained from the IR camera during tension tests at 50 mm/min (top) and 5 mm/min (bottom) at different cross-head displacements: (a) neck initiation (b) 10 mm (c) 20 mm (d) 30 mm (e) 40 mm (f) 50 mm (g) 60 mm (h) 70 mm.

Having obtained the plastic strain, the plastic strain rate is obtained. The experimental data are smoothed using a moving average. The expected rate of temperature rise can now be calculated from the stress and plastic strain rate using

$$\frac{\mathrm{d}T}{\mathrm{d}t} = TQC\frac{\sigma}{\rho C_p}\frac{\mathrm{d}\varepsilon_p}{\mathrm{d}t} \tag{7}$$

This can be compared to the value of $\mathrm{d}T/\mathrm{d}t$ measured using the thermal camera (experiment), or output directly from Abaqus (simulation) The ratio of the measured value of $\mathrm{d}T/\mathrm{d}t$ to calculated value of $\frac{\sigma}{\rho C_p}\frac{\mathrm{d}\varepsilon_p}{\mathrm{d}t}$ therefore gives the value of TQC. The variation of the TQC with time, or strain, is very interesting and because it peaks at a value greater than 1, indicates that energy is stored in the specimen before being released as heat. This analysis does not take into account heat transfer within the specimen (or indeed radiation from the specimen surface). Hence, it is instructive to compare the experimental data to equivalent calculations using the model outputs, in which these effects are implicitly considered. Here, it is remembered that the model used TQC = 0.9, with a modified density. Comparison of the data, particularly Fig. 21(c) and (c') shows that whilst a more detailed analysis is required, the observed increase in the TQC above 1, in the experimental data, does appear to reflect a material response, and is not just an artefact of the experiment. Further work is required on this.

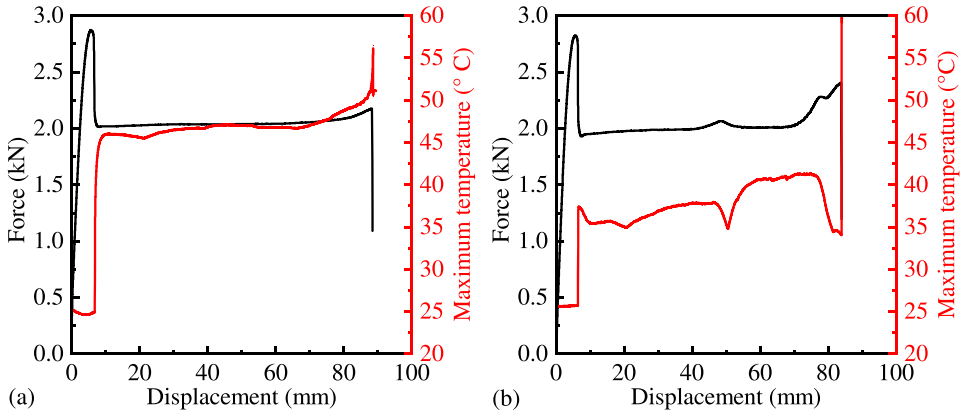

Fig. G2. Force-displacement curves and maximum temperature-displacement curves for tension tests at (a) 50 mm/min and (b) 5 mm/min.

8. Conclusions

The large strain tensile response of polycarbonate has been investigated using tensile experiments instrumented with Digital Image Correlation (DIC) system and an infrared (IR) camera. In all experiments, a shear band was observed; combined with relaxation in the rest of the specimen and load chain, this causes a very high strain rate at the point of initial yielding. As the plastic deformation propagates from this initial shear band, a lower strain rate deformation is observed sequentially at points along with the specimen. A significant temperature rise (~24 °C in experiments at 50 mm/min) is observed during this plastic deformation. Using a combination of DIC and axial load measurements, it is possible to produce stress-strain curves for the material; however, these are highly dependant on the assumptions used to calculate the strains perpendicular to the loading axis.

Using one of the experiments at 50 mm/min as an example, a constitutive model was calibrated. The calibration was initially based on compression test data. When applied to a finite element (FE) simulation of the tensile experiment, there was an excellent agreement with the load-displacement behaviour, but not with local strain-time data obtained from different points on the specimen. This indicates that tensile force-displacement curves are not a good validation (or calibration) of constitutive models. Instead, the model parameters were updated to make it match the strain-time contours. A parametric study was then performed, which confirmed again that the force-displacement data are weakly dependant on the constitutive parameters, whilst the strain-time curves are highly dependant. The temperature rises predicted by the FE model thus obtained were shown to have very good agreement with those from the experiments. A preliminary study of heat generation in the specimen was performed.

Fundamentally, the tensile test is not only a test of constitutive behaviour, but also of structural response. Hence local and global behaviours must be considered in order to separate these responses if model parameters are to be obtained.

Data availability

All data supporting this study will be made openly available from the Oxford University Research Archive at: DOI: 10.5287/bodleian:R8apaQJ9g

CRediT authorship contribution statement

Peihao Song: Conceptualization, Methodology, Investigation, Formal analysis, Writing – original draft. **Akash Trivedi:** Methodology, Investigation, Writing – review & editing. **Clive R Siviour:** Conceptualization, Project administration, Supervision, Writing – review & editing, Funding acquisition.

Declaration of competing Interest

The authors declare that they have no known competing financial interests or personal relationships that could have appeared to influence the work reported in this paper.

Data availability

All data supporting this study will be made openly available from the Oxford University Research Archive at DOI: 10.5287/bodleian:R8apaQJ9g.

Acknowledgments

This research forms part of the research programme of DPI, project 827t19, *Impact Modelling of Polymers: high-Rate Experiments for Solid-state Simulations* and the materials were kindly supported by Saudi Basic Industries Corporation (SABIC). The authors thank our colleagues on this project, Dr David Chapman in the Solid Mechanics Group at the University of Oxford, for useful suggestions on thermal analysis, and Dr Davide De Focatiis and Grace Owen at the University of Nottingham for helpful discussions. We are very grateful for the support of Nick Hawkins for DMA and DSC experiments, and to the technicians of the Solid Mechanics Group (especially Andy Bateman) for specimen preparation.

For the purpose of Open Access, the authors have applied a CC BY public *copyright license to* any Author Accepted Manuscript (AAM) version arising from this submission.

Appendix A. DIC and IR setup

Table A1

Appendix B. Constitutive model (Bergstrom, 2012)

The deformation gradient for network A can be decomposed into elastic and viscoplastic components as,

$$F = F_A^e F_A^v \tag{B1}$$

The Cauchy (true) stress loading on network A is simulated using a temperature-dependant eight-chain model (Arruda and Boyce, 1993):

$$\sigma_A = \frac{\mu_A}{J_A^e \overline{\lambda_A^{e*}}}\left[1+\frac{\theta-\theta_0}{\widehat{\theta}}\right]\frac{\mathscr{L}^{-1}\left(\overline{\lambda_A^{e*}}/\lambda_L\right)}{\mathscr{L}^{-1}(1/\lambda_L)}\mathrm{dev}\left[b_A^{e*}\right]+\kappa\left(J_A^e-1\right)1 \tag{B2}$$

Here μ_A is the shear modulus of network A, $J_A^e = det[F_A^e]$, $\lambda_L$is the locking limitation of the chain, θ and θ_0 are the current temperature and reference temperature, respectively, $\widehat{\theta}$ is a material property representing the relationship between temperature and stiffness, $b_A^{e*} = (J_A^e)^{-2/3}F_A^e(F_A^e)^T$ is the Cauchy-Green deformation tensor, $\overline{\lambda_A^{e*}} = (\mathrm{tr}[b_A^{e*}]/3)^{1/2}$ is the effective chain stretch length according to the eight-chain theory (Arruda and Boyce, 1993), $\mathscr{L}^{-1}(x) = \coth(x) - 1/x$ is the inverse Langevin function, κ is the bulk modulus.

Similarly, the stress acting on network B is also separated into elastic and viscoplastic components $F = F_B^e F_B^v$, and the Cauchy stress for network B is based on the same eight-chain assumptions used for network A:

$$\sigma_B = \frac{\mu_B}{J_B^e \overline{\lambda_B^{e*}}}\left[1+\frac{\theta-\theta_0}{\widehat{\theta}}\right]\frac{\mathscr{L}^{-1}\left(\overline{\lambda_B^{e*}}/\lambda_L\right)}{\mathscr{L}^{-1}(1/\lambda_L)}\mathrm{dev}\left[b_B^{e*}\right]+\kappa\left(J_B^e-1\right)1 \tag{B3}$$

In this equation, the definition of the initial parameters is the same as network A. However, the effective shear modulus of network B is evaluated with plastic strain from an initial value of μ_{Bi} to the final value of μ_{Bf} as

$$\dot{\mu}_B = -\beta\left[\mu_B - \mu_{Bf}\right]\cdot\dot{\gamma}_A. \tag{B4}$$

The model can hence capture the evolution from yielding to large strain flow.

The stress loading on network C is calculated using the eight-chain model with first-order I_2 dependence, whose representation is similar to the Mooney-Rivlin model with non-Gaussian chain statistics (Boyce and Arruda, 2000),

$$\sigma_C = \frac{1}{1+q}\left\{\frac{\mu_C}{J\lambda_{chain}}\left[1+\frac{\theta-\theta_0}{\widehat{\theta}}\right]\frac{\mathscr{L}^{-1}(\lambda_{chain}\backslash\lambda_L)}{\mathscr{L}^{-1}(1\setminus\lambda_L)}\mathrm{dev}[b^*]+\kappa(J-1)1+q\frac{\mu_C}{J}\left[I_1^* b^* - \frac{2I_2^*}{3}I-(b^*)^2\right]\right\} \tag{B5}$$

where the definition of *J, b** and λ_{Chain} are the same as the network A and B, and the magnitude of the I_2 dependence is dominated by q.

The total Cauchy stress in this model is the sum of the stresses in these three networks,

$$\sigma = \sigma_A + \sigma_B + \sigma_C \tag{B6}$$

For the rate kinematics of this material model, the effective deviatoric flow rate of network A is estimated using the power-flow equation,

$$\dot{\gamma}_A = \dot{\gamma}_0\cdot\left(\frac{\tau_A}{\widehat{\tau}_A + aR(p_A)}\right)^{m_A}\cdot\left(\frac{\theta}{\theta_0}\right)^n \tag{B7}$$

where$\dot{\gamma}_0 \equiv 1/s$ is a constant introduced for dimensional consistency, $p_A = -[(\sigma_A)_{11}+(\sigma_A)_{22}+(\sigma_A)_{33}]/3$ is the hydrostatic pressure, $R(x) = (x+|x|)/2$ is the ramp function, and $\widehat{\tau}_A$, *a*, m_A and *n* are material parameters. In addition, the velocity gradient of the viscoelastic flow of network A is presented as,

$$\dot{F}_A^v = \dot{\gamma}_A F_A^{e-1} \frac{\mathrm{dev}[\sigma_A]}{\tau_A} F \tag{B8}$$

The total velocity gradient of network B can be predicted as similar to the network A,

$$\dot{\gamma}_B = \dot{\gamma}_0 \cdot \left(\frac{\tau_B}{\widehat{\tau}_B + aR(p_B)} \right)^{m_B} \cdot \left(\frac{\theta}{\theta_0} \right)^n \tag{B9}$$

and the definition of $\dot{\gamma}_0$, $\widehat{\tau}_B$, p_B, a, m_A and n are similar to network A. Moreover, the velocity gradient of the viscoelastic flow of network B is,

$$\dot{F}_B^v = \dot{\gamma}_B F_B^{e-1} \frac{\mathrm{dev}[\sigma_B]}{\tau_B} F \tag{B10}$$

Appendix C. FE model

The mesh sensitivity is investigated using the global mesh size of 0.8, 1, 1.3 and 2 mm with the element type of C3D8T. The Point Neck, 10 and 20 mm from this neck point are extracted as an example to show that the simulation results are independent of the mesh size using this element type.

Fig. C1

Appendix D. Dynamic mechanical analysis (DMA) results

Fig. D1

Appendix E. Modulated Differential Scanning Calorimetry (MDSC) result

Fig. E1

Appendix F. The effects of network C related parameters on large strain deformation

Fig. F1
Fig. F2

Appendix G. Thermal images at different loading speeds

Fig. G1
Fig. G2

References

Arruda, E.M., Boyce, M.C., 1993. A three-dimensional constitutive model for the large stretch behavior of rubber elastic materials. J. Mech. Phys. Solids 41, 389–412.
Bergstrom, J.S., 2012. PolyUMod–a library of advanced user materials. Veryst Engineering. LLC, Needham, Mass, USA.
Bergstrom, J.S., 2015. Mechanics of Solid polymers: Theory and Computational Modeling. Elsevier, Amsterdam, The Netherlands.
Bergstrom, J.S., Bischoff, J.E., 2010. An advanced thermomechanical constitutive model for UHMWPE. Int. J. Struct. Chang. Solids 2 (1), 31–39.
Boyce, M.C., Arruda, E.M., 1990. An experimental and anaiytical investigation of the large strain compressive and tensile response of glassy polymers. Polym. Eng. Sci. 30, 1288–1298.
Boyce, M.C., Arruda, E.M., 2000. Constitutive models of rubber elasticity: a review. Rubber Chem. Technol. 73, 504–523.
Boyce, M.C., Arruda, E.M., Jayachandran, R., 1994. The large strain compression, tension, and simple shear of polycarbonate. Polym. Eng. Sci. 34, 716–725.
Boyce, M.C., Parks, D.M., Argon, A.S., 1988. Large inelastic deformation of glassy polymers. Part I: rate dependent constitutive model. Mech. Mater. 7, 15–33.
Buckley, C.P., Dooling, P.J., Harding, J., Ruiz, C., 2004. Deformation of thermosetting resins at impact rates of strain. Part 2: constitutive model with rejuvenation. J. Mech. Phys. Solids 52, 2355–2377.
Buckley, C.P., Jones, D.C., 1995. Glass-rubber constitutive model for amorphous polymers near the glass transition. Polymer 36, 3301–3312 (Guildf).
Dattoma, V., Giancane, S., 2013. Evaluation of energy of fatigue damage into GFRC through digital image correlation and thermography. Compos. Part B Eng. 47, 283–289.
De Focatiis, D.S.A., Embery, J., Buckley, C.P., 2010. Large deformations in oriented polymer glasses: experimental study and a new glass-melt constitutive model. J. Polym. Sci. Part B Polym. Phys. 48, 1449–1463.
Grytten, F., Daiyan, H., Polanco-Loria, M., Dumoulin, S., 2009. Use of digital image correlation to measure large-strain tensile properties of ductile thermoplastics. Polym. Test. 28, 653–660.
Hasan, O.A., Boyce, M.C., 1995. A constitutive model for the nonlinear viscoelastic viscoplastic behavior of glassy polymers. Polym. Eng. Sci. 35, 331–344.
Haward, R.N., 1994. Heating effects in the deformation of thermoplastics. Thermochim. Acta 247, 87–109.
Haward, R.N., Thackray, G., 1968. The use of a mathematical model to describe isothermal stress-strain curves in glassy thermoplastics. Proc. R. Soc. Lond. Ser. A Math. Phys. Sci. 302, 453–472.

Jordan, B., Gorji, M.B., Mohr, D., 2020. Neural network model describing the temperature-and rate-dependent stress-strain response of polypropylene. Int. J. Plast. 135, 102811.
Klompen, E.T.J., Engels, T.A.P., Govaert, L.E., Meijer, H.E.H., 2005. Modeling of the postyield response of glassy polymers: influence of thermomechanical history. Macromolecules 38, 6997–7008.
Knauss, W.G., Zhu, W., 2002. Nonlinearly viscoelastic behavior of polycarbonate. II. The role of volumetric strain. Mech. Time Depend. Mater. 6, 301–322.
Krairi, A., Doghri, I., 2014. A thermodynamically-based constitutive model for thermoplastic polymers coupling viscoelasticity, viscoplasticity and ductile damage. Int. J. Plast. 60, 163–181.
Kweon, S., Benzerga, A.A., 2013. On the localization of plastic flow in glassy polymers. Eur. J. Mech. A Solids 39, 251–267.
Lei, M., Hamel, C.M., Chen, K., Zhao, Z., Lu, H., Yu, K., Qi, H.J., 2021. Thermomechanical behaviors of polyether ether ketone (PEEK) with stretch-induced anisotropy. J. Mech. Phys. Solids 148, 104271.
Li, H.X., Buckley, C.P., 2009. Evolution of strain localization in glassy polymers: a numerical study. Int. J. Solids Struct. 46, 1607–1623.
Li, H.X., Buckley, C.P., 2010. Necking in glassy polymers: effects of intrinsic anisotropy and structural evolution kinetics in their viscoplastic flow. Int. J. Plast. 26, 1726–1745.
Lin, P., Liu, J., Wang, S.Q., 2016. Delineating nature of stress responses during ductile uniaxial extension of polycarbonate glass. Polymer 89, 143–153 (Guildf).
Lu, J., Ravi-Chandar, K., 1999. Inelastic deformation and localization in polycarbonate under tension. Int. J. Solids Struct. 36, 391–425.
Manual, A.U., 2021. Abaqus user manual. Abaqus.
Maquin, F., Pierron, F., 2009. Heat dissipation measurements in low stress cyclic loading of metallic materials: from internal friction to micro-plasticity. Mech. Mater. 41, 928–942.
Meijer, H.E.H., Govaert, L.E., 2005. Mechanical performance of polymer systems: the relation between structure and properties. Prog. Polym. Sci. 30, 915–938.
Parsons, E., Boyce, M.C., Parks, D.M., 2004. An experimental investigation of the large-strain tensile behavior of neat and rubber-toughened polycarbonate. Polymer 45, 2665–2684 (Guildf).
Rueda, F., Torres, J.P., Machado, M., Frontini, P.M., Otegui, J.L., 2015. External pressure induced buckling collapse of high density polyethylene (HDPE) liners: FEM modeling and predictions. Thin Walled Struct. 96, 56–63.
SABIC, 2021. LEXAN™ resin 103R Europe technical data sheet.
Shen, F., Kang, G., Lam, Y.C., Liu, Y., Zhou, K., 2019. Thermo-elastic-viscoplastic-damage model for self-heating and mechanical behavior of thermoplastic polymers. Int. J. Plast. 121, 227–243.
Siviour, C.R., Jordan, J.L., 2016. High strain rate mechanics of polymers: a review. J. Dyn. Behav. Mater. 2, 15–32.
Soloukhin, V.A., Brokken-Zijp, J.C.M., van Asselen, O.L.J., de With, G., 2003. Physical aging of polycarbonate: elastic modulus, hardness, creep, endothermic peak, molecular weight distribution, and infrared data. Macromolecules 36, 7585–7597.
Tervoort, T.A., Smit, R.J.M., Brekelmans, W.A.M., Govaert, L.E., 1997. A constitutive equation for the elasto-viscoplastic deformation of glassy polymers. Mech. Time Depend. Mater. 1, 269–291.
Torres, J.P., Frontini, P.M., 2016. Mechanics of polycarbonate in biaxial impact loading. Int. J. Solids Struct. 85, 125–133.
Torres, J.P., Frontini, P.M., Machado, M., Major, Z., 2016. Deformation and failure of semicrystalline polymers under dynamic tensile and biaxial impact loading. Int. J. Impact Eng. 98, 52–61.
Tvergaard, V., Needleman, A., Lo, K.K., 1981. Flow localization in the plane strain tensile test. J. Mech. Phys. Solids 29, 115–142.
Van Breemen, L.C.A., Klompen, E.T.J., Govaert, L.E., Meijer, H.E.H., 2011. Extending the EGP constitutive model for polymer glasses to multiple relaxation times. J. Mech. Phys. Solids 59, 2191–2207.
Wu, P.D., van der Giessen, E., 1995. On neck propagation in amorphous glassy polymers under plane strain tension. Int. J. Plast. 11, 211–235.
Zhang, R., Bai, P., Lei, D., Xiao, R., 2018. Aging-dependent strain localization in amorphous glassy polymers: from necking to shear banding. Int. J. Solids Struct. 146, 203–213.